Ref. Ares(2023)356440 - 17/01/2023

esteem3

Enabling Science through European Electron

First report on TEM methods applied to materials for energy

Deliverable D8.3 – version 0.9

Estimated delivery date: December 2022

Actual delivery date: January 2023

Lead beneficiary: CAD, JSI

Person responsible: Susana Trasobares and Miran Ceh

Deliverable type: ☒ R ☐ DEM ☐ DEC ☐ OTHER ☐ ETHICS ☐ ORDP

Dissemination level: ☒ PU ☐ CO ☐ EU-RES ☐ EU-CON ☐ EU-SEC

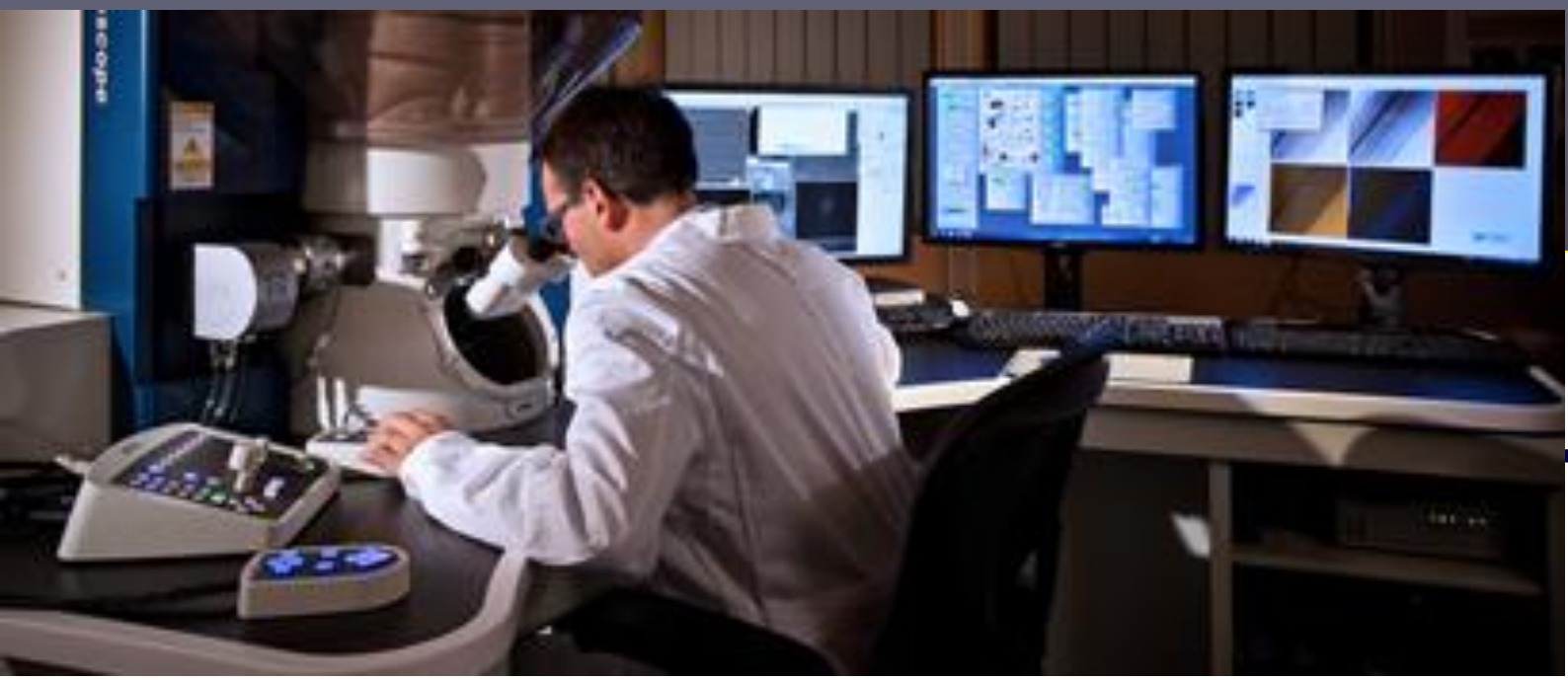

THIS PROJECT HAS RECEIVED FUNDING FROM THE EUROPEAN UNION'S HORIZON 2020 RESEARCH AND INNOVATION PROGRAMME UNDER GRANT AGREEMENT NO **823717**

Grant Agreement No:	823802
Funding Instrument:	Research and Innovation Actions (RIA)
Funded under:	H2020-INFRAIA-2018-1: Integrating Activities for Advanced Communities
Starting date:	01.01.2019
Duration:	54 months

DRAFT VERSION

Table of contents

Revision history log 3

Context of the present report 4

Task 8.1 Nanomaterials for Sustainable Development 4

Task 8.3: Characterization of Devices for Energy Applications 8

Task 8.4: Sample Preparation of Materials for Energy 19

References 21

Revision history log

Version number	Date of release	Author	Summary of changes
V0.1	13/12/2022	S. Trasobares	Template
V0.2	20/12/2022	C. Ducati	CAM additions
V0.3	20/12/2022	A. Kruczek	AGH additions
V0.4	21/12/2022	S. Boninelli	CAT additions
V0.5	28/12/2022	S. Trasobares	UCA additions and edition
V0.6	03/01/2023	M. Čeh	LJU additions and edition
V0.7	03/01/2023	S Trasobares	UCA additions and edition
V0.8	16/01/2023	L. Guilloteau	Editing
V0.9	17/01/2023	P.A. van Aken	Approval

DRAFT VERSION

Context of the present report

Quoted from the proposal:

"Spectroscopy and imaging techniques for quantitative structural and chemical characterization of materials will be applied to a range of energy materials. This WP will use in-situ capabilities to perform dynamic characterisation of materials for energy and will develop sample preparation recipes specific to these systems, including the key issue of anaerobic sample environments for new battery materials".

Deliverable D8.3 belongs to WP8 Materials for Energy. In this work package four different task have been included. Here we describe the progress carried out in every task.

Task 8.1 Nanomaterials for Sustainable Development

1. 3D hierarchically structured $Ce_{1-x}Gd_xO_{2-x/2}$, Au confinement and its effect on the catalytic properties

Advanced electron microscopy techniques have been used to characterise the hierarchical architecture of mixed ceria particles ($Ce_{1-x}Gd_xO_{2-x/2}$) with applications on catalytic propane and soot oxidation. The influence of temperature and dopant concentration on the micro- to macroscale structure of the star-shaped particles has been thoroughly investigated. It appeared that presence of dopant changes the pattern of nanoparticles intergrowth which ultimately introduces additional porosity into 3D hierarchically structured material (r_{av} =19 nm). Furthermore, substantial increase of propane conversion via low-temperature surface oxidation mechanism was ascribed to nanocrystallites mesoscale organization forming porous hierarchical material. No such conversion was observed on non-organized ceria nanoparticles.

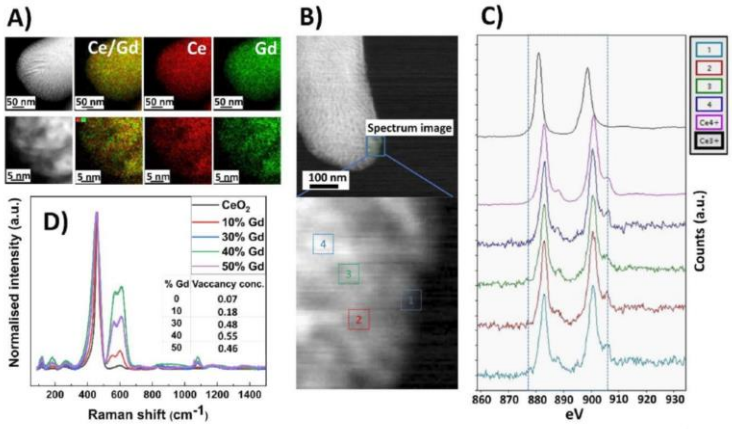

Figure 1.- A) HAADF-STEM (left) and EDS elemental mapping (Ce: red, Gd: green) images of the $Ce_{0.9}Gd_{0.1}O_{1.95}$ star-shaped particle arm (top) and high magnification area of the arm (bottom); B) DF image of the $Ce_{0.9}Gd_{0.1}O_{1.95}$ star-shaped particle arm (top) and individual areas used in EELS analysis (bottom); C) EELS spectra collected from individual regions of the $Ce_{0.9}Gd_{0.1}O_{1.95}$ star-shaped particle arm; D) Raman spectra of the $Ce_{1-x}Gd_xO_{2-x/2}$ (x= 0; 0.1; 0.3; 0.4; 0.5) star-shaped particles; oxygen vacancy concentration presented in insert. (extracted from https://doi.org/10.1016/j.materresbull.2022.111816) [1]

In addition, gold has been incorporated into various configurations of ceria nanostructures. Several merits of the material architecture such as the (1) surface area and porosity, (2) mutual arrangement of support crystallites, (3) nanoparticle confinement, (4) optimal size of nano-gold particles, and (5) increased metal–support contact were identified and discussed to explain the observed effect of the

DRAFT VERSION

enhanced catalytic activity. The nano-sized nature of gold was confirmed by high-resolution STEM imagining, showing a high population of Au particles (from 2 to 6 nm) in the near-surface region of the arm (figure 1). Electron tomography slices at different angles show that the high intensity contrast zones, indicating the position of gold, change their shape with a change in the recording angle. This was observed in a series of images (from 70° to 122°, insets in Figure. 1E and F), where a single high-intensity spot was broken down into three smaller spots with an elongated shape with a change in the angle. This again confirms that Au NPs were deposited along the pores inside the hierarchical support. Due to the extensive porosity induced by the structural hierarchy and Au nanoparticles confinement, exceptional surface reducibility was observed, and the CO oxidation temperature shifted to the ambient regime (T50 = 18 °C) as compared to that of the gold-decorated nanocubes (T_{50} = 85 °C). In addition, the hierarchical catalysts showed substantial propane oxidation facilitation (T_{50} = 370 °C) as compared to that of the gold-decorated non-hierarchical catalysts (T_{50} = 480 °C).

This work has been performed via TA access, project HSMCO.

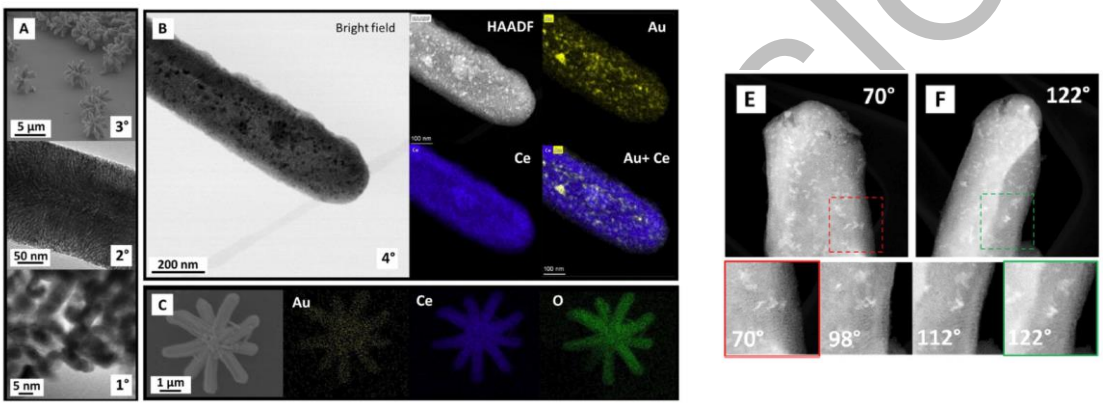

Figure 2.- Hierarchical architecture of Au/CeO_2 catalyst: A) TEM images showing three levels of hierarchical organization of CeO_2 support. B) TEM bright-field image of selected arm of Au/CeO_2 catalyst with corresponding HAADF image and XEDS maps of Au and Ce elemental distribution. C) SEM image of star-shaped Au/CeO_2 catalyst with corresponding SEM-EDS elemental maps of Au, Ce, and O.E and F) HR-STEM images of Au NPs in the near-surface region. E) and F) HAADF images collected at various angles during the electron tomography series (selected images presented on the bottom) (extracted from doi:10.1039/d2cy01214f) [2]

2. Layered amorphous *a*-SnO_2 gas sensors

2D-layered amorphous *a*-SnO2 is utilized for the first time to detect NO_2, H_2 and NH_3 gases at 100 ◦C operating temperature opening new perspectives for the exploitation of amorphous metal-oxides interfaces for gas sensing applications. Liquid-phase exfoliated 2D-$SnSe_2$ flakes have been subjected to controlled oxidation in air (from 1 h to 170 h) at temperatures below the crystallization temperature of SnO_2 (200 ◦C) yielding template self-assembled, amorphous *a*-SnO_2 thin-layers (10–40 nm thick) grown over 2D-$SnSe_2$. A suitable oxidation process has been optimized by “in operando” monitoring the base line resistance (BLR) while changing the annealing conditions, demonstrating that at least 48 h at 200 ◦C are required to stabilize BLR, corresponding to the formation of a self-terminating *a*-SnO_2 oxide with excellent BLR and sensor’s signal reproducibility over one year. Humidity cross-response on gas sensing demonstrated that increasing the relative humidity (RH@25 ◦C) from dry air to 80%, (Rg/Ra) to 1 ppm NO_2 increases from 2.2 to 5.7 while (Ra/Rg) to 100 ppm H_2 and NH_3 decreases from 2.7 to 1.7 and from 1.8 to 1.6 (σ ± 0.2). A preliminary ab-initio DFT modelling of water adsorption over an amorphous *a*-SnO_2 highlighted that dissociative adsorption is thermodynamically favoured. The thin film sensor’s conduction model, comprising stacked layers of *a*-SnO_2/$SnSe_2$ flakes, is explained by the

DRAFT VERSION

formation of Schottky barriers between the flakes. The seamless texture of an amorphous *a*-SnO_2 skin with no grain-boundaries, no crystal-planes orientations, greatly simplify gas-sensing mechanisms assumptions, paving the way for a new class of "layered amorphous metal-oxides gas-sensors" (*LAMOS*).[3]

This work has been performed via TA access, project LAMOS.

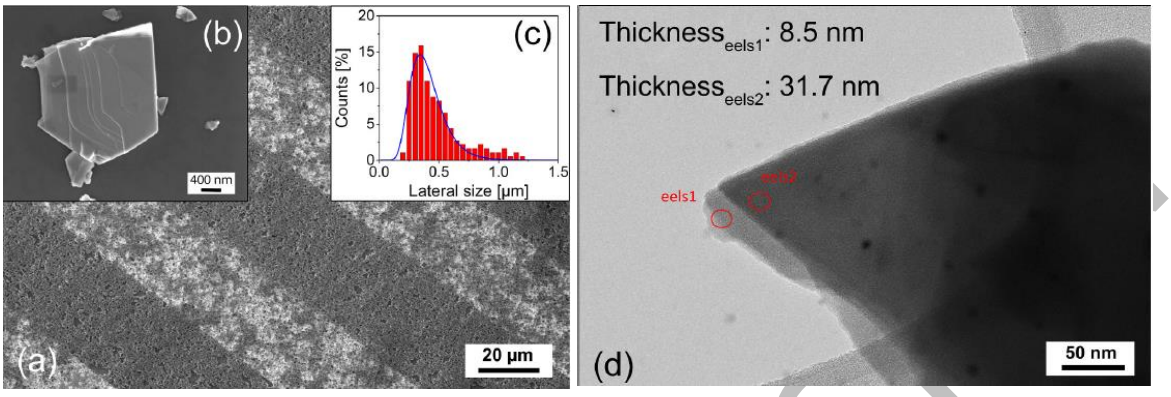

Figure 3. (a) SEM of the Si_3N_4 substrate with finger type Pt electrodes (light regions) with spin coated deposited $SnSe_2$ flakes; (b) high-resolution SEM of staked as-exfoliated $SnSe_2$ flakes; (c) lateral size distribution of the $SnSe_2$ flakes; (d) HRTEM of stacked as-exfoliated flakes with thicknesses corresponding to the red circles.

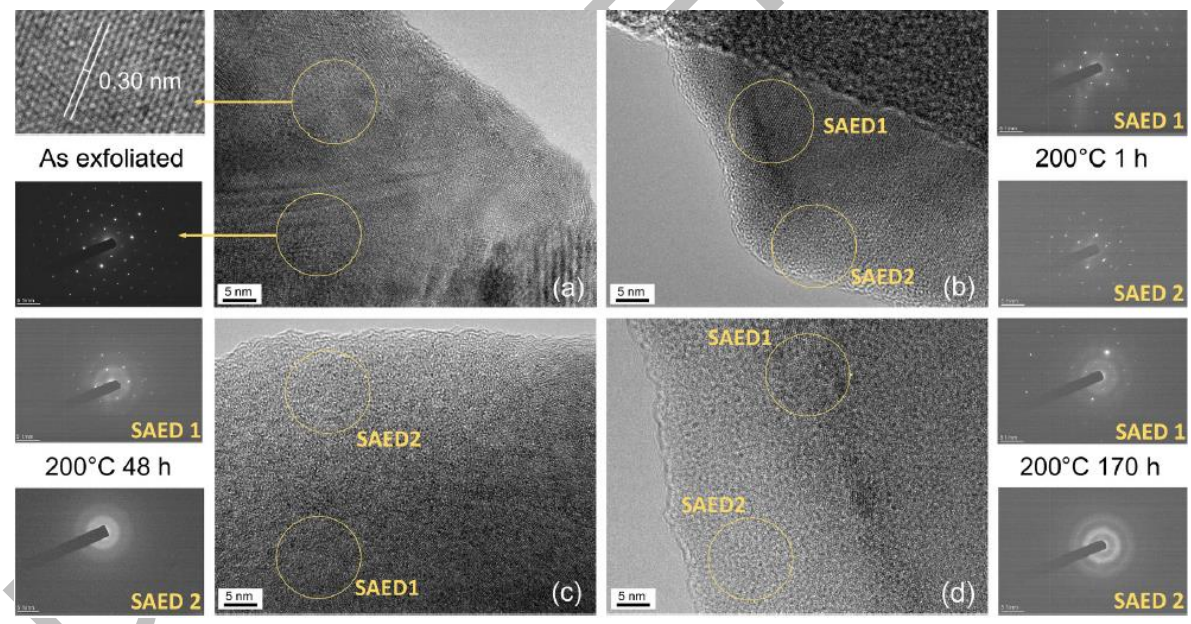

Figure 4. HRTEM images and related SAED patterns of the: (a) as exfoliated $SnSe_2$ flake; (b) 1 h; (c) 48 h; (d) 170 h annealed $SnSe_2$ flakes in air at 200 ◦C.

3. Effect of Au loading on Schottky barrier height in plasmonic photocatalysts

Composites of TiO_2 nanoparticles and different amounts of plasmonic noble metal Au (0.25–2 wt%) were synthesized by employing the wet impregnation technique. The results of SEM, TEM, XRD and N_2 physisorption analyses reveal that the morphologies of the prepared composites are similar to the morphology of bare TiO_2 support and are not influenced by the increasing amount of deposited Au nanoparticles. On the other hand, the size of Au ensembles in the TiO_2 + Au composites increased from 27.1 to 54.9 nm with the increasing amount of Au. With the increase of the diameter of Au ensembles, the intensity of the surface plasmon resonance (SPR) effect of Au ensembles in the UV–Vis diffuse reflectance spectra of the composites increased. The X-ray photoelectron spectroscopy (XPS) analysis of the valence band maxima (VBM) of the investigated photocatalysts revealed that the height of the Schottky barrier (SBH) at the Au/TiO_2 junction in the investigated TiO_2 + Au composites decreased from 0.4 to 0.15 eV with the increasing amount of Au (and their size). [4]

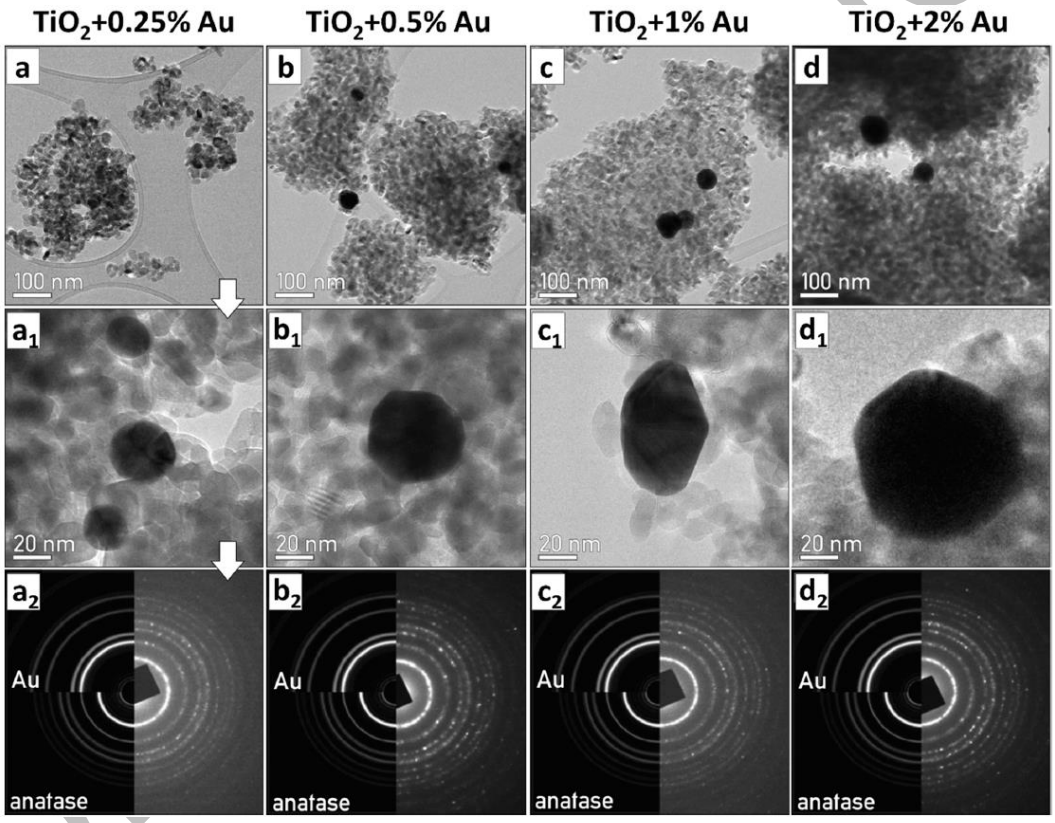

Figure 5. (a-d) and (a1-d1) TEM micrographs of investigated TiO_2 + Au composites obtained at different magnifications. (a2-d2) TEM experimental selected area electron diffraction (SAED) patterns of prepared TiO_2 + Au composites with simulated patterns of anatase TiO_2 and Au.

4. Scalmalloy®

Scalmalloy® is the first aluminium powder alloy specifically designed to be processed by Selective Laser Melting (SLM) under certified conditions. Samples in the as-built condition and after a heat treatment at 325° C for 4 hours as indicated by the powder manufacturer to achieve the best mechanical properties are studied. The focus has been put on tensile tests, hardness measurements, electrical

conductivity, and, especially, SEM-EBSD and TEM to study and quantify grain size, texture, grain boundaries misorientation, and dislocation density.

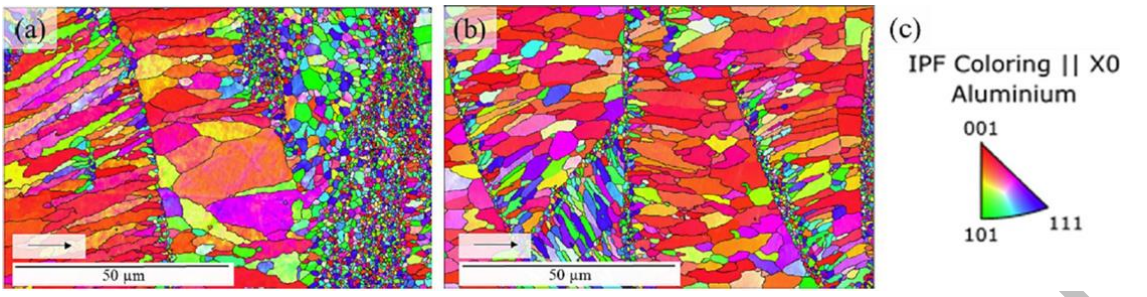

Figure 6. EBSD-derived IPF maps in the building direction (arrow direction) of the specimens (a) as-built and (b) heat-treated. (c) IPF colour legend (taken from https://doi.org/10.1016/j.matchar.2022.112549). [5]

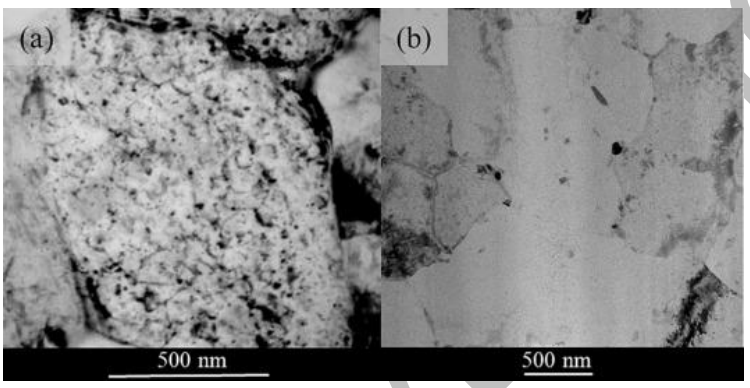

Figure 7. Conventional TEM imaging of a grain for as-built (a) and heat-treated (b) samples. (taken from https://doi.org/10.1016/j.matchar.2022.112549). [5]

The main results are summarized as: (1) As-built samples show Portevin-Le-Chatelier effect (PLC), while heat-treated do not. (2) Electrical conductivity increases from 20.47 to 23.94 (%IACS) after heat treatment. (3) Grain size and texture of CGZ and FGZ do not change when the material is heat-treated. (4) LAGB/HAGB ratio is 50/50 and 20/80 before and after the heat treatment, respectively. (5) Heat-treated condition shows homogeneous dislocation density ca. $3.4 \cdot 10^{14}$ disloc.·m^{-2}.

Task 8.3: Characterization of Devices for Energy Applications

The following classes of devices for energy applications will be investigated within this task: Thermoelectric generators, Power, RF and energy storage applications, Materials for advanced energy systems.

Materials for advanced energy systems

Materials for advanced energy systems such as steam-generation, low footprint and “zero-emission” conventional power plants with increased efficiency need to incorporate new materials capable for operation at ultra-supercritical or advanced ultra-supercritical steam conditions in a temperature range up to 750°C for 100000 hours. Within this task, materials for advanced energy systems including fossil fuel power plants, clean coal technologies, nuclear power plants, renewables, smarts grids and energy storage will be investigated with new TEM techniques developed within WP4 and WP5.

DRAFT VERSION

1. Defects reduction by laser annealing on ion implanted 4H-SiC

Laser irradiation has been demonstrated has a pioneering method for gaining substantial control over the inhibition of defects formation in P and Al implanted 4H-SiC epitaxial layers. Through High Angle Annular Dark Field (HAADF) and Medium Angle (MA)-STEM investigations, the presence of regions with higher density of C_i defects in response to laser annealing treatments was revealed. A comparison with 4H-SiC subjected to thermal annealing was done.

Figure 8 reports TEM images of the sample exposed to laser annealing at 0.60 J/cm^2 (Figure. 8b) and to furnace annealing at 1650 °C for 30', as a reference (Figure. 8a). The sample subjected to conventional annealing exhibits a network of dislocation loops associated to the P doping, as a result of point-defect aggregation promoted by high-temperature annealing under thermal equilibrium conditions. The 550 nm deep region is affected by rear aggregates and follows the lower Al implant concentration. These defects, with average size around tens of nm, were identified as Si-C doublets generated because of the availability of C and Si interstitials in the lattice, mostly owing to the collisional damage caused by the ion implantations processes.

Laser annealed sample (Figure 8b) reveals the absence of dislocation loops along the whole implanted region, while the typical diffraction pattern in the [11-20] zone axis demonstrates that both processes preserve the crystallinity. Thus, it can be concluded that, while shorter diffusion periods result in narrower dislocation loop size distributions, the thermal out of equilibrium regime does not enable C interstitials diffusion times adequate for prismatic dislocation loop nucleation.

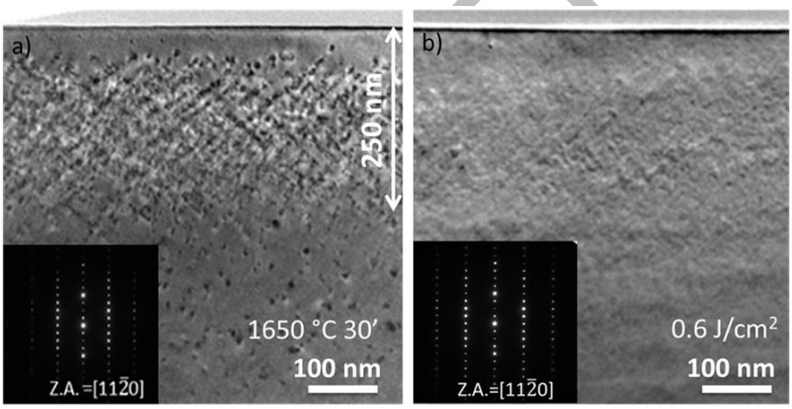

Figure 8. Bright Field XTEM images and diffractions from a) 1650 °C 30' thermally annealed sample and b) 0.6 J/cm2 1000 shots/point laser annealed sample.

To investigate in better detail the crystallographic structure of laser-annealed materials, we conducted atomic-resolved HAADF and LA STEM investigations. As can be seen in Figure 9, no extra-planes were identified within the implanted lattice along the [0001] direction and nor along [11-20]. High Angle Annular Dark Field in Figure 9b, demonstrate that the whole region of the implant maintains the 4H-SiC stacking without inclusion of extra planes, nor any Z-contrast due different chemical species. However, as underlined by the LA-STEM, regions with varying contrast arise, owing to small crystalline matrix deformations. At low scattering angles, the diffraction contrast essentially becomes stronger than the Z contrast, allowing any changes in the geometry of the polytype to be highlighted.

DRAFT VERSION

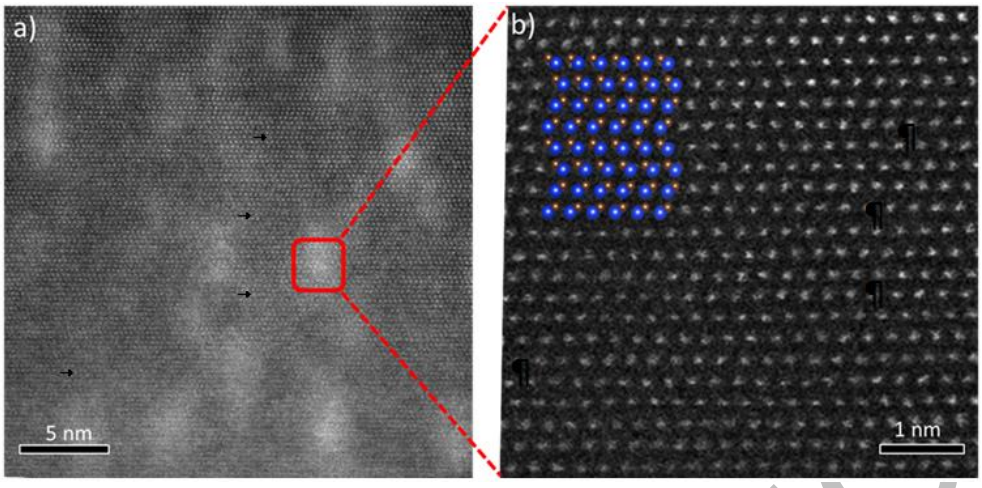

Figure 9. a) LA-STEM of implanted 4H-SiC epitaxial layers and b) HAADF-STEM related to the area in red square with a higher concentration of point defects with VESTA simulation of 4H-SiC atomic stacking under [11$\bar{2}$0] zone axis.

As a result, the implantation zone is revealed to be defined by regions with varying densities of point defects, where the short annealing duration prevents the reorganization and insertion of these defects in the form of additional planes, as seen with furnace annealing.

In conclusion, our investigation on the implanted region confirms the inhibition of extended defects in the implanted regions during laser annealing, giving rise instead to regions with higher density of point defects revealed through the comparison between HAADF and MA STEM analysis.

2. Oxidation behaviour and scale formation in modern nickel-based superalloy produced via powder metallurgy route

Aircraft engines and their operation are in a constant chase for higher efficiency and emission reduction. While some modifications in design are possible, the ongoing demand for superalloys with increased high-temperature capabilities limits thermal efficiency improvements. New materials with higher strength levels are needed to reduce the size and weight of the aircraft engine components. Polycrystalline nickel-based superalloys obtain the highest mechanical properties and application temperatures from manufacturing via the powder metallurgy (P/M) route due to high volumes of strengthening γ’ phase. However, the drawback of P/M superalloys is usually lower high-temperature oxidation resistance.

In this study, we have investigated the oxidation resistance of a new-generation P/M superalloy ME16 and the influence of the oxidizing temperature on the near-surface microstructure. Methods for this study included analytical electron microscopy combined with FIB-SEM tomography. The tomographic and STEM-EDXS analyses were performed at AGH-UST, while EELS analyses were carried out at Cadiz University.

In the as-received state, before oxidation, the ME16 microstructure is present in Figure 10. It is composed mainly of γ’ precipitates with some primary carbides. The γ’ phase in ME16 superalloy comes in trimodal distribution, with different sizes and morphologies. The primary γ'_p phase has a size of a few microns and an irregular shape. It is formed during subsolvus solution treatment, typical for powder metallurgy superalloys. The secondary γ'_s phase has a diameter of roughly 200 nm, and a

DRAFT VERSION

cuboidal shape, while the tertiary γ'_t phase comes in the form of spherical particles with a diameter of about 20 nm. Both secondary and tertiary γ' precipitates are formed during ageing treatment – secondary ones during 1st step of ageing at a higher temperature and tertiary ones during 2nd step of ageing at a lower temperature. The SEM-EDXS analyses revealed that the ME16 superalloy γ'-Ni_3Al phase is enriched in cobalt and tantalum, as present in spectrum s1 taken from primary γ'_p precipitate. Cobalt should substitute nickel on the faces of the fcc unit cell, while tantalum substitutes aluminium in the corners of the cell. Furthermore, SEM-EDXS analyses revealed differences in the chemical composition of primary MC-type carbides. Larger carbides had a spherical size and a diameter of 2 microns and were enriched in Mo, and W. Smaller carbides with a diameter of about 500 nm were enriched in Nb and Ta.

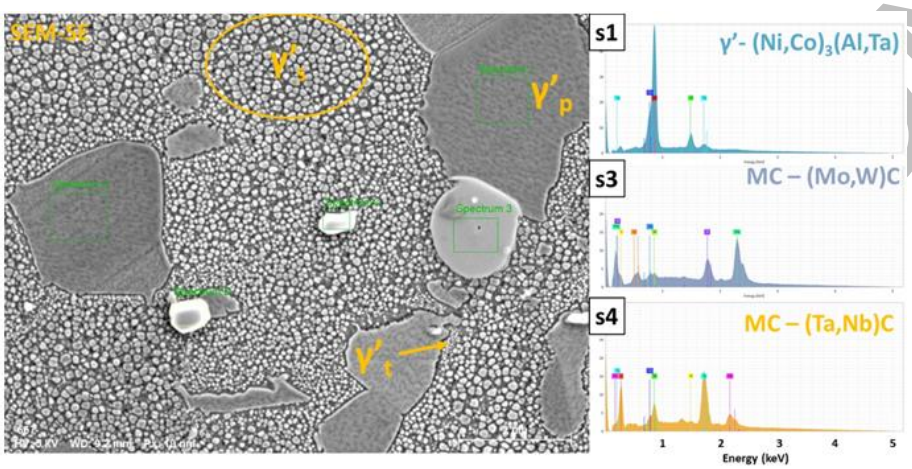

Figure 10. SEM-SE image of ME16 superalloy microstructure before oxidation along with SEM-EDXS spectra from selected areas marked in SEM image.

Figure 11 shows TEM images of lamellae cut from ME16 superalloy oxidized for 1000 hours at 730 °C. The images of the full oxide scale and internal oxidation zone are visible in TEM-BF (Figure 11a) and STEM-HAADF (Figure 11b). After 1000 hours, the main oxide scale was less than 2 µm thick. It was composed mainly of chromium and chromium-rich oxides, as shown in Figure 11c. The outermost part of the oxide scale consists of large crystals of Ti-rich oxides. Beneath it, a pretty continuous layer of Co-rich oxides was formed with a thickness of less than 200 nm. Both elements are oxidized quicker than chromium. Notably, the Co-rich oxide layer is enriched with Cr, indicating spinel formation, e.g., $CoCr_2O_4$ or $CrCo_2O_4$. Beneath it, the principal nanocrystalline chromia scale was formed with a thickness of less than 1 µm.

Beneath the oxide scale, an internal oxidation zone was formed, with alumina growing into the bulk material. Notably, both primary and secondary γ' precipitates were dissolved within it. The red dashed line in Figure 11d indicates the possible location of the primary γ' precipitate. As shown by FIB-SEM tomography (Figure 12), grain boundaries accelerate the growth of alumina into the bulk material.

DRAFT VERSION

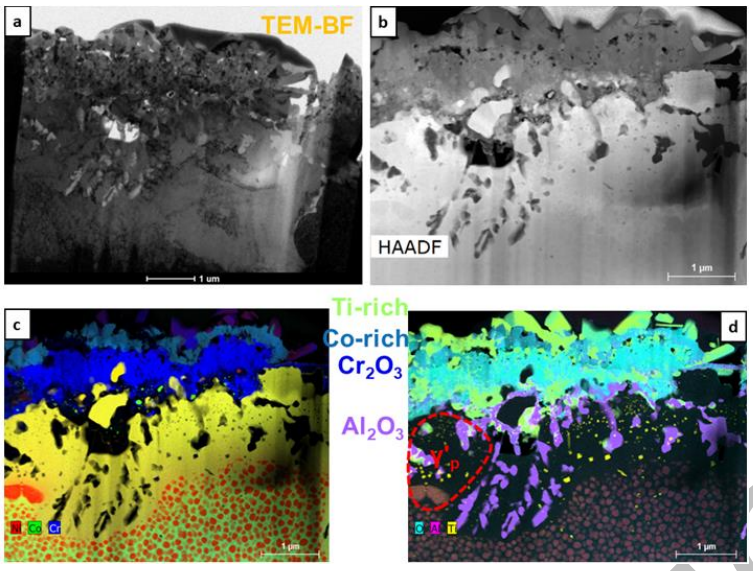

Figure 11. Lamellae of the near-surface area of ME16 superalloy oxidized for 1000 hours at 730 °C. a) TEM-BF image of the lamellae; b) STEM-HAADF image of the lamellae; c) Compositional STEM-EDXS elemental distribution map of Ni, Co, and Cr in the lamellae; d) Compositional STEM-EDXS elemental distribution map of O, Al, and Ti in the lamellae.

The FIB-SEM tomography (slice-and-view technique) was done from a sequence of about 300 slices with 16 nm spacing between them. The red frame in the SEM-BSE image highlights the thinnest part of the oxide scale, whereas the primary γ' precipitate is present beneath it. This indicates that its presence locally slows oxide scale formation. The black dashed line in the "front view" indicates the cut-off plane in the "bottom view." In the bottom view, accelerated growth of the oxide scale at the grain boundaries is visible.

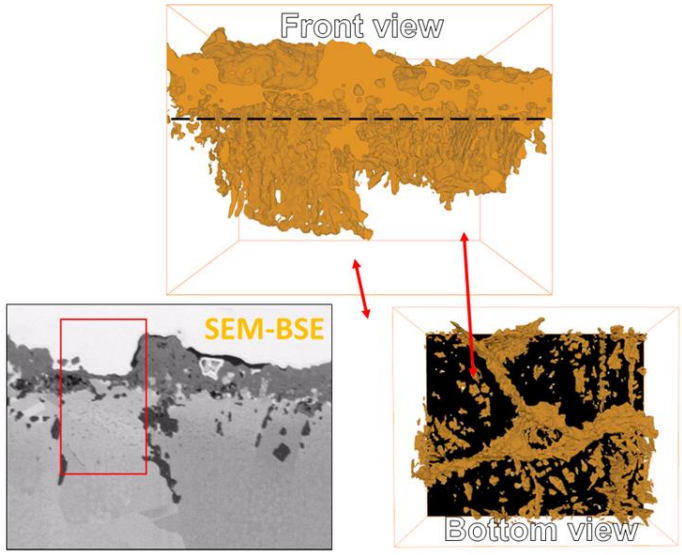

Figure 12. FIB-SEM tomographic reconstruction of oxides in the near-surface area of ME16 superalloy oxidized for 1000 hours at 730 °C.

Further analyses of the oxide scale were performed using electron EELS. Figure 13 shows a STEM-HAADF image of the FIB lamellae from ME16 superalloy after 1000 hours of oxidation at 730 °C with marked areas, where EELS analyses were performed. Within each area, multiple analyses were performed as shown in the ADF image. EELS elemental distribution maps of area a were generated using Cr-$L_{2,3}$, Ti-$L_{2,3}$, and O-K edges. Significant differences within the oxide scale are visible in STEM-

DRAFT VERSION

EELS elemental distribution maps. As shown previously in STEM-EDXS maps, a dual-layered oxide scale was formed. The inner part of the oxide scale is more Cr-rich than the outer part, which is enriched in Co. Moreover, randomly distributed Ti-rich oxides are on top of the oxide scale. The highest oxygen concentration was detected in Ti-rich oxides; scale oxygen was more uniformly distributed within the oxide. Table 1 presents a quantitative analysis of points 1 to 8 marked in the ADF image. Points 1, 4, and 5 were located at the top part of the oxide layer. Within these points, a high concentration of Ti was detected.

Table 1. Results of quantitative EELS analyses (at %).

Zone	Cr(at %)	O(at %)	Ti(at %)	Cr(at %)	O(at %)	O/Cr
1	0	66.6	33.4			
4	15.2	69.9	14.9	17.9	82.1	4.59
5	3.8	63.4	32.8	5.7	94.3	18.86
2	35.4	63.8	0.82	35.7	64.3	1.8
6	33.2	65.9	0.88	33.5	66.5	1.99
7	31.1	65.4	3.5	32.2	67.8	2.11
3	38.9	58.2	3	40.1	59.9	1.49
8	39.5	58.7	1.8	40.2	59.8	1.49

Furthermore, point one was taken purely from titanium oxide TiO_2 with a model Ti/O ratio of 2:1. In points 4 and 5, some amount of Cr was detected, although it was instead an overlapping of oxides than Cr enrichment in TiO_2. The chemical composition of other points consists mainly of Cr and O with trace amounts of Ti. It has to be underlined that other elements than these three were not measured. Points 2, 6, and 7 displayed different O/Cr ratios than points 3 and 8. Notably, points 3 and 8 were located at the bottom part of the oxide scale while 2, 6, and 7 were in the middle part. The O/Cr ratio in the bottom part was 3:2, which confirms the formation of Cr_2O_3. The O/Cr ratio in the middle part was 2:1, which can be found in spinel $CoCr_2O_4$. Further analyses and previous ones from STEM-EDXS confirm these assumptions.

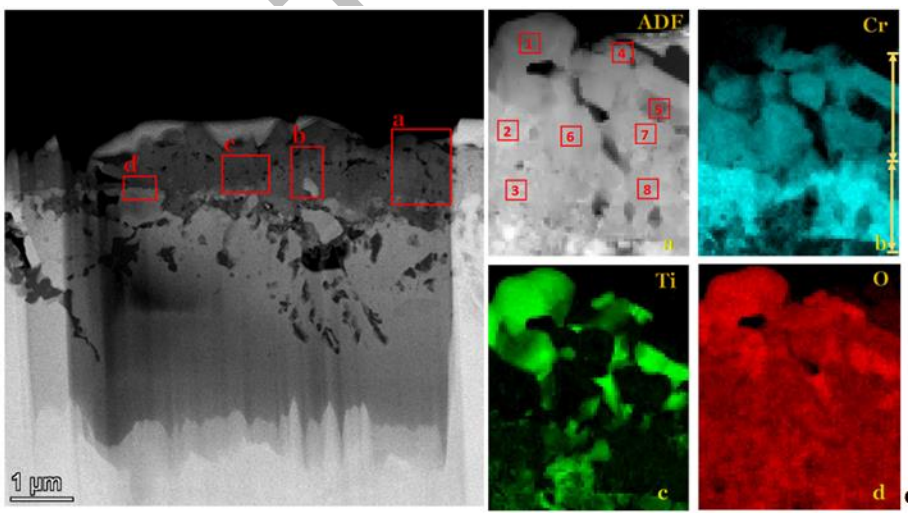

Figure 13. Lamellae of the near-surface area of ME16 superalloy oxidized for 1000 hours at 730 °C. a) Angular dark-field image of area marked with a red box a; b) STEM-EELS elemental distribution map of Cr; c) STEM-EELS elemental distribution map of Ti; d) STEM-EELS elemental distribution map of O.

Figure 14 shows exemplary EELS profiles for different phases, acquired from the area marked as (d) in Figure 13. The EELS profiles of Cr-$L_{2,3}$ edges in both oxides, so Cr_2O_3 and $CoCr_2O_4$ had a similar shape. As expected, higher intensity of these edges was detected in Cr_2O_3. Some amount of Cr was detected

DRAFT VERSION

in the γ matrix near the oxide scale (marked as CoNi). Here, an energy shift toward lower values was detected, suggesting a change in the valence state.

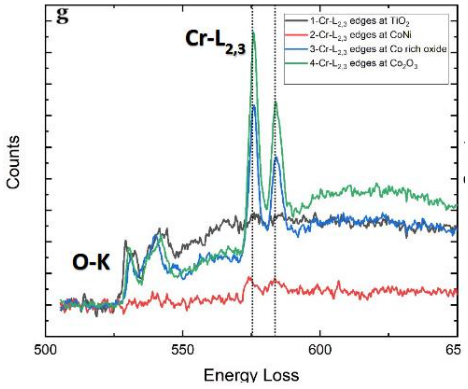

Figure 14. EELS profiles of O-K and Cr-L2,3 edges acquired from points in area d in Fig.13.

Finally, spectroscopy data was combined with atomic scale imaging via HRSTEM-HAADF. The analyses were performed near the interface between Co- and Cr-rich parts of the oxide scale, as indicated in Figure. 13. It is worth mentioning that significant porosity was observed along the interface, which is visible best in STEM-EDXS elemental maps in Figures 11 and 13. Furthermore, Ti-rich areas were observed near the porous region. This Ti-rich area was identified as TiO_2, as revealed by a detailed HRSTEM-HAADF analysis (Fig. 11). Further analysis of the bottom part of the interface confirmed the presence of Cr_2O_3 as the main component of the oxide scale (Fig. 13).

EELS and HRSTEM analyses were performed at the University of Cadiz within a Joint Research Action.

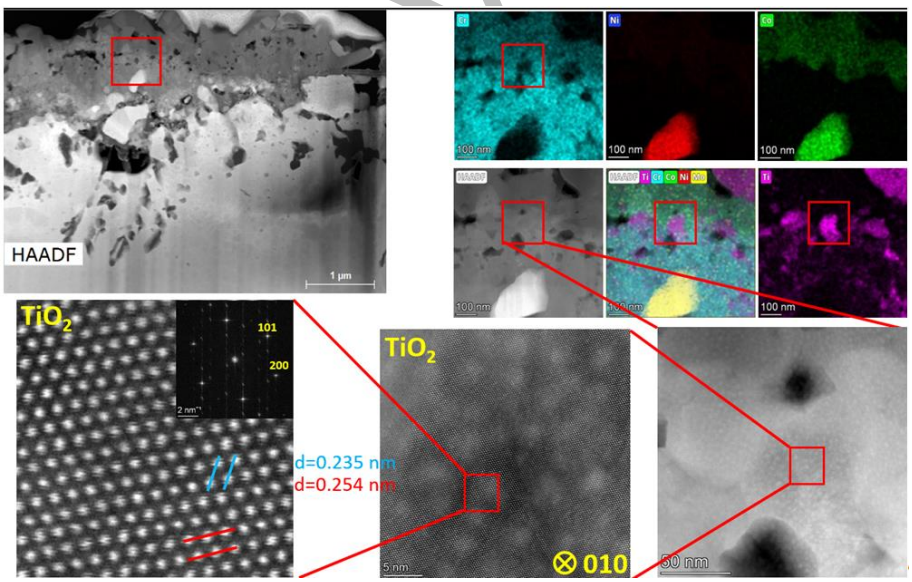

Figure 15. HRSTEM-HAADF/EDXS analysis of rutile at the interface of Co- and Cr-rich parts of the oxide scale.

DRAFT VERSION

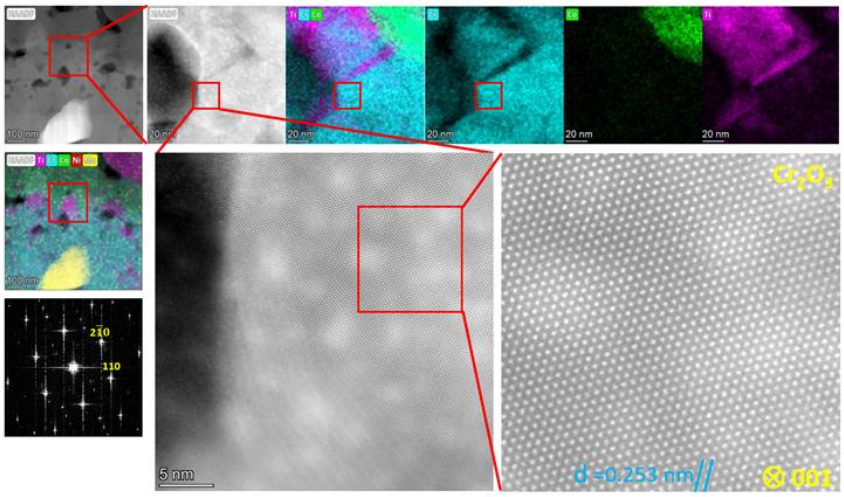

Figure 16. HRSTEM-HAADF/EDXS analysis of chromia scale.

3. Intragranular cracking in layered lithium-transition metal oxide cathodes (CAM-TRO)

Li-ion batteries have a pivotal role in the transition towards electric transportation. Ni-rich layered transition metal oxide cathode materials promise high specific capacity and lower cost but exhibit faster degradation compared to lower Ni alternatives. **Inter**granular cracking of these materials has been widely studied as one of the degradation mechanisms. Using high resolution STEM imaging, EELS and EDS mapping, we investigated the nanoscale origins and importance of **intra**granular cracking (within primary crystals) of cathode materials cycled under controlled conditions. TEM specimens were prepared by FIB milling.

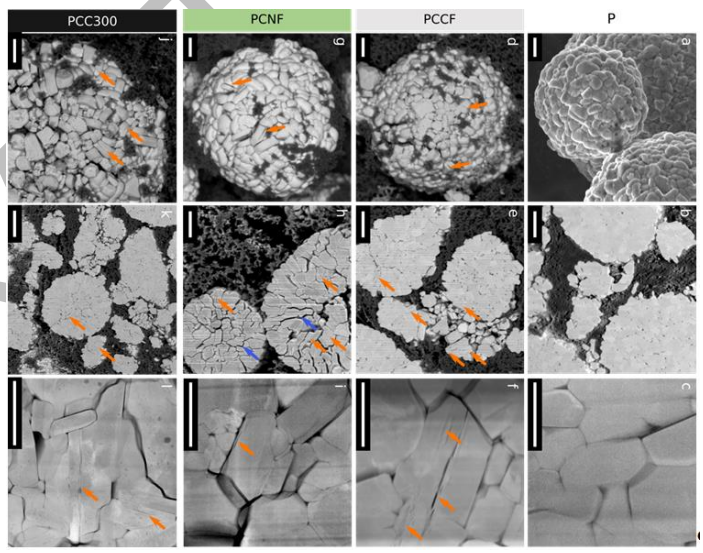

Figure 17. Representative SEM and HAADF-STEM images of pristine powder (P, a), calendered pristine electrode (P, b-c); calendered, formed and charged to 4.3 V (PCCF, d-f); non-calendered formed and charged to 4.3 V (PCNF, g-i) and calendered, formed, cycled 300 times, and charged to 4.3 V (PCC300, j-l) polycrystalline NMC811 samples. Orange arrows point towards primary particles with signs of intragranular cracking. Blue arrows in (h) highlight intragranular cracking. [7]

DRAFT VERSION

We found that intragranular cracking is widespread in charged specimens since the very first cycles, but it is uncommon in discharged samples even after extensive cycling. We determined that the distribution of intragranular cracks is highly inhomogeneous. We conclude that intragranular cracking is caused by local stresses that can have several independent sources: layered and rock-salt phase interfaces, transition metal and Li inhomogeneities, and forces exerted by neighbouring particles. In contrast to previous literature, our results suggest that inter- and intragranular cracks can manifest at different points of life of the cathode and are not found to be immediately deleterious to performance. [6, 7]

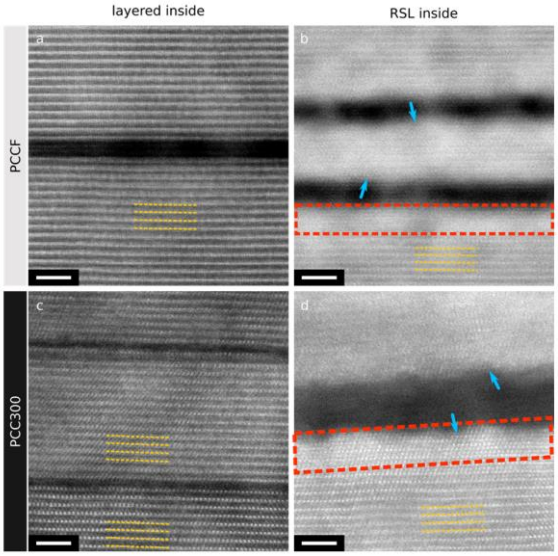

Figure 18. HAADF-STEM images of crystal lattices of NMC811 samples: (a-b) PCCF, (c-d) PCC300. Left column shows representative examples of intragranular cracks with a layered structure at their inner surfaces, while the right column shows examples of cracks in which the inner surface has transformed into an RSL. Scale bar in all images is 2 nm and they are shown at the same magnification. Yellow dashed lines highlight the layered structure in vicinity of intragranular cracks. Red dashed rectangles highlight reconstructed RSL at the inner surfaces of intragranular cracks. Blue arrows point towards irregular inner surfaces of cracks that have undergone transformation to RSL.[7]

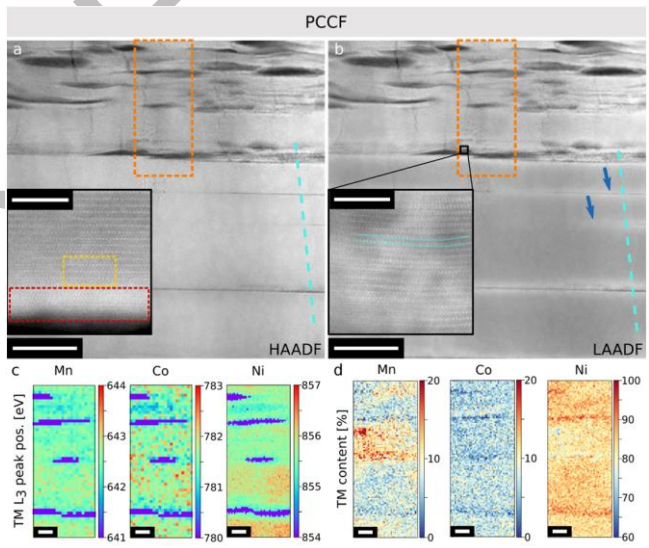

Figure 19. ADF-STEM images and EELS and EDX maps of PCCF sample. (a) HAADF-STEM image highlighting the EDX/EELS mapped area, (b) LAADF-STEM image with blue arrows highlighting strained regions. Insets are both HAADF images. Inset in (a) is from the bottom edge of this crystal (not shown in a-b). Inset in (b) comes from the region marked with the small black square. (c) EELS TM L_3 peak position maps for Mn, Co and Ni. (d) EDX maps of TM distribution for Mn, Co and Ni. Scale bar in (a-b) 50 nm, insets in (a,b) 5 nm, (c-d) 10 nm. Teal dashed lines highlight the direction of ion beam during FIB milling. [7]

DRAFT VERSION

4. W/W_2C composite for nuclear fusion reactor

Tungsten-tungsten carbide (W/W_2C) composites are considered as possible structural materials for future nuclear fusion reactors. We studied the effect of helium (He) implantation on microstructure evolution of polycrystalline W/W_2C composite consolidated by field-assisted sintering technique (FAST), homogenously implanted at room temperature with 1 MeV 4 He^+ ions at the fluence of 8 ×10^{16} ions cm^{-2} and annealed at 1873 K for 20 minutes. Samples were analysed by scanning and transmission electron microscopy to study the presence and size of He bubbles. Monomodal He bubbles in W (30-80 nm) are limited to point defects and grain boundaries, with a considerable void denuded zone (150 nm). Bubbles do not form in W_2C, but at the W|W_2C interface and are considerably larger (200-400 nm). The experimental observations on He behaviour and migration in W and W_2C were assessed by density functional theory (DFT) calculations, suggesting He migration and accumulation in the composite are determined by the effective He-He binding in clusters, which will give rise to decohesion. In the presence of He clusters, the decohesion of bulk W into free surfaces is energetically highly favourable but not sufficient in the W_2C; hence bubbles are only observed in W grains and interfaces and not within bulk W_2C.[8]

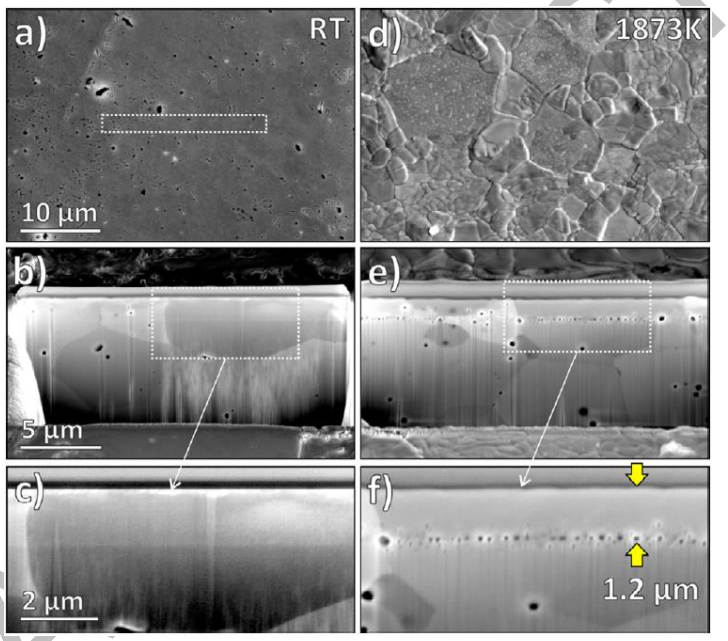

Figure 20. Secondary electron (SE) SEM micrographs: (a) the irradiated sample surface, with a marked area for the FIB cross-section. (b) The enhanced contrast inside a single W grain coincides with the He implantation depth; with the magnified marked region in (c). The same FIB cross-section was investigated after the annealing; (d) the surface of the sample was recorded in the immediate vicinity of the original cross-section, as the location in (a) was already etched by FIB. The observation of the same cross-section in (b) after the annealing (d) show that the bubble network developed at a depth of implantation damage peak at 1.2 µm; the marked region is magnified in (f).

DRAFT VERSION

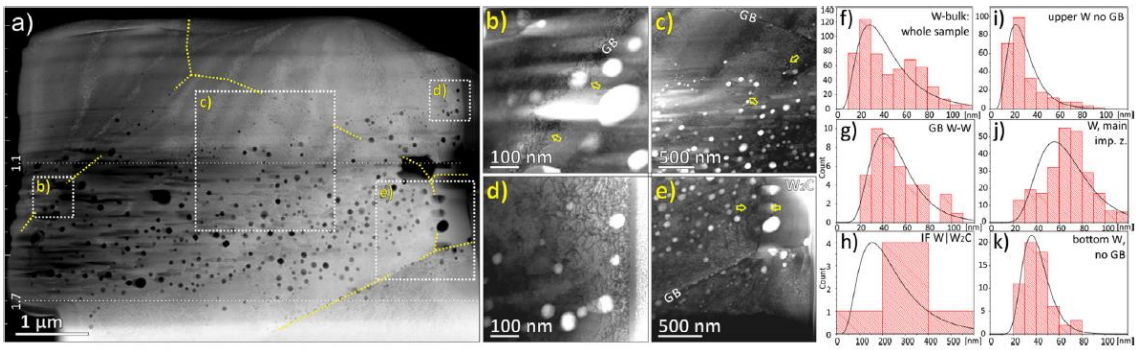

Figure 21. a) HAADF-STEM overview micrograph, with marked GBs (yellow lines) and regions of BF-STEM insets (white squares): b) bubbles at the W-W GB; c) bubbles outside the main implantation zone are limited to GBs (yellow arrows); d) He bubbles in the W grain outside main implantation zone, near sample surface; e) large elongated bubbles on inclined W|W_2C interface (arrows mark upper and bottom contact). Ferret diameter of bubbles per different regions; f) entire analysed sample, g) only bubbles on the W-W grain boundaries, h) bubbles on W|W_2C interface, i) upper W without GB, j) all bubbles in the main W implantation zone, k) bubble size below the main implantation zone.

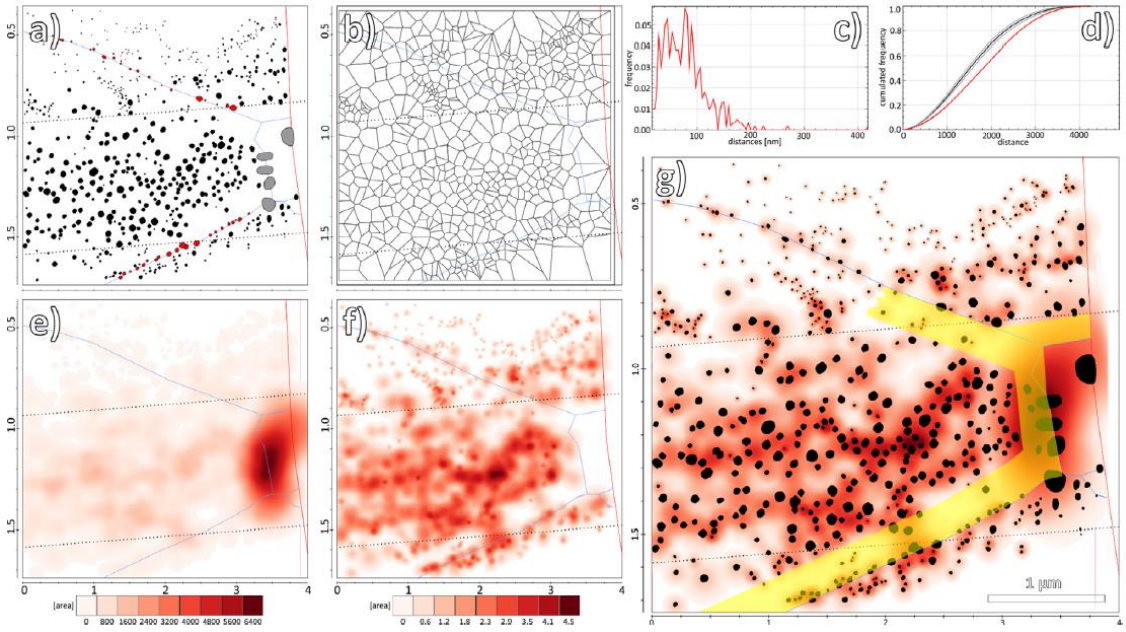

Figure 22. (a) Spatial distribution of bubbles (N = 615), red bubbles are on the W-W grain boundaries; blue lines mark the grain and phase boundaries, and dotted near-horizontal lines mark the main implantation zone. (b) Voronoi diagram, with underlined main features from TEM micrographs. (c) The cumulative distribution function of the distance between a bubble and its nearest neighbour. (d) Bubble distribution pattern compared to Spatial Distribution Index - a normalized measure of the difference between the observed point distribution and a completely random one. The black line indicates the average distribution for random patterns, the grey lines indicate the 95 % confidence interval, and the red line corresponds to the distribution of the observed bubble pattern. The observed distribution lies right of the confidence interval, indicating a clustered organization. (e) Heat map based on Kernel Density Estimation, with an area of underlying bubbles as weight; (f) same, but calculated without the bubbles on the W|W 2 C interface, to enhance the influence of the GBs and defects. g) Cumulative heat map and bubble outlines; yellow zone marks the 150 nm thick void denuded zone developed next to GBs.

DRAFT VERSION

5. Anodic Memristors Grown on Hf–Nb Combinatorial Thin-Film Alloys

The development of novel materials with coexisting volatile threshold and non-volatile memristive switching is crucial for neuromorphic applications. Hence, the aim of this work was to investigate the memristive properties of oxides in Hf–Nb thin-film combinatorial system deposited by sputtering on Si substrates. The active layer was grown anodically on each Hf–Nb alloy from the library, whereas Pt electrodes were deposited as the top electrodes. The devices grown on Hf-45 at.% Nb alloys showed improved memristive performances reaching resistive state ratios up to a few orders of magnitude and achieving multi-level switching behaviour while consuming low power in comparison with memristors grown on pure metals. The coexistence of threshold and resistive switching is dependent upon the current compliance regime applied during memristive studies. Such behaviours were explained by the structure of the mixed oxides investigated by TEM. The mixed oxides, with HfO_2 crystallites embedded in quasi amorphous and stoichiometrically non-uniform Nb oxide regions, were found to be favourable for the formation of conductive filaments as a necessary step toward memristive behavior.

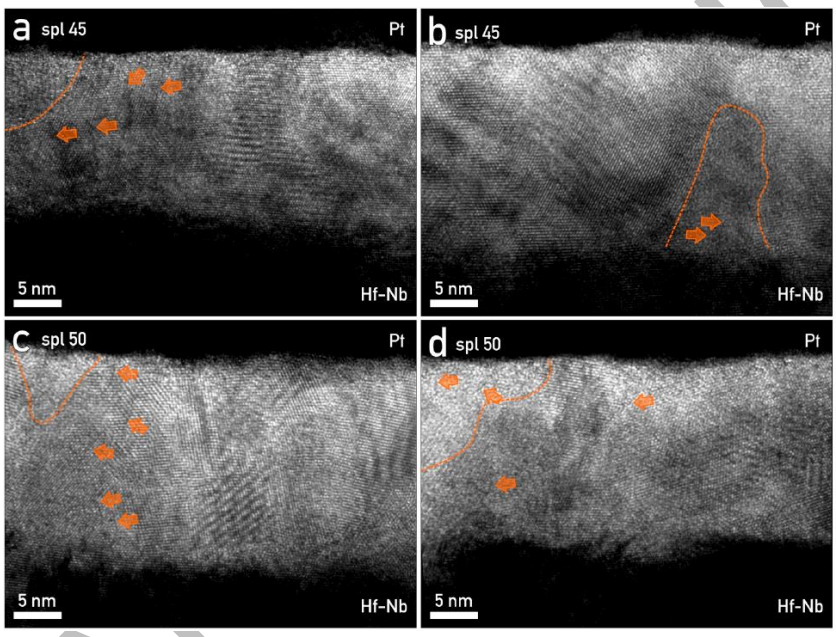

*Figure 23. HR-TEM micrographs of Hf–Nb oxide layer. (**a**,**b**) Sample Hf-45 at.% Nb, (**c**,**d**) sample Hf- 50 at.% Nb. Crystalline HfO_2 was sporadically interrupted by amorphous Nb_2O_5 regions (outlined with a dashed orange line). The conductive filaments emerging from metal layers are marked by orange arrows.[9]*

Task 8.4: Sample Preparation of Materials for Energy

Within this task, different methods for TEM sample preparation of materials/devices for energy applications will be optimised.

1. Aerosol jet printing of battery electrodes for in situ electrochemical TEM

We investigated a new approach for deposition of materials on *in situ* EC TEM chips based on aerosol jet printing (AJP). The principle is schematically shown in Figure 24.

DRAFT VERSION

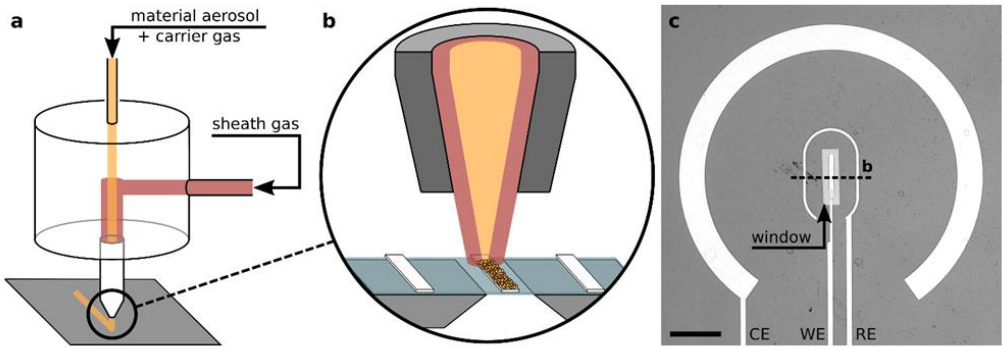

Figure 24. Schematic of the aerosol jet printing approach for ec-TEM sample preparation. (a) Schematic of the print head, where material aerosol (yellow) and sheath gas (red) are fed into the nozzle. (b) Close-up schematic of the aerodynamic focusing of the ink aerosol, which is used to print fine lines on ec-TEM chips. The chip is made of silicon (grey), has a suspended silicon nitride membrane (blue) and electrical contacts patterned on top of it (white). (c) Optical microscope image of a commercial ec-TEM chip (Protochips ECT-24). Scale bar – 200 µm. Platinum electrical contacts (white) are arranged so that they can be used as a working electrode (WE), counter electrode (CE) and pseudo-reference electrode (RE). The WE is extending over a rectangular silicon nitride window. Dashed line indicates a region that is schematically represented in (b).[10]

This approach can be used to deposit conventional, industrially relevant battery materials (NMC811, LTO, SuperP conductive carbon) starting from powders, with high spatial resolution (line width <30 µm) and in arbitrary, pre-defined shapes. Moreover, materials can be either deposited as a mixture, or sequentially in layers of different composition. In [3] we demonstrated important implications of the size selectivity of aerosol jet printing to the deposition of materials with a broad range of particle sizes, resulting in a thin layer of particles <1 µm in size, which is advantageous for EC-TEM sample imaging, see figure 25.

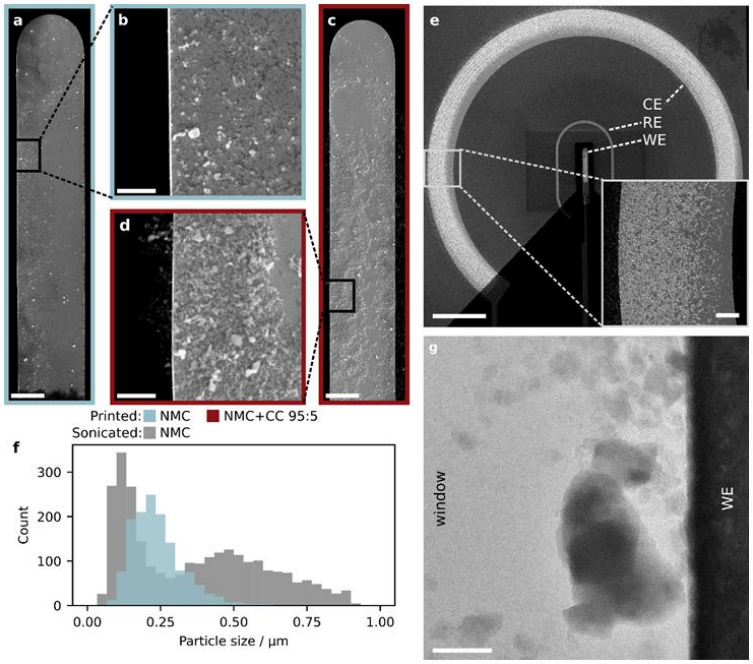

Figure 25. SEM micrographs of aerosol jet printed lines on the working electrode of a Protochips ec-TEM chip. (a-b) Neat NMC811 ink (240 passes), (c-d) Conductive carbon ink followed by NMC811 ink (50 and 80 passes respectively). Scale bars in (a) and (c) are 10 µm, (b) and (d) are 2 µm. (e) Low magnification SEM micrograph of ec-TEM chip showing printed neat NMC working electrode and LTO+CC counter electrode. Scale bar 200 µm and 20 µm for the image inset. The electrodes are labelled as CE (counter electrode, Pt with printed LTO), RE (reference electrode, clean Pt contact) and WE (working electrode, Pt with printed NMC). (f) Histograms comparing the particle size of the sonicated and printed NMC. (g) Bright field TEM micrograph of the edge of a printed electrode showing NMC particles over the SiN_x window (scale bar 200 nm) The Pt contact is labelled as WE. [10]

DRAFT VERSION

The combination of the versatility, flexibility, size selectivity, positioning accuracy and spatial resolution make aerosol jet printing a very promising candidate for in situ or *operando* TEM sample preparation. Moreover, a similar approach may enable other opportunities in a wide variety of studies where high-resolution material deposition is required. This method establishes a new path towards more reliable sample preparation for a range of TEM chip geometries and for a variety of energy materials.

REFERENCES

[1] P. Wozniak, M. A. Małecka, L. Chinchilla, S. Trasobares. 3D hierarchically structured Ce1-xGdxO2-x/2 mixed oxide particles: the role of microstructure, porosity and multi-level architecture stability in soot and propane oxidation. *Materials Research Bulletin* 151 (2022) 111816. https://doi.org/10.1016/j.materresbull.2022.111816

[2] P. Wozniak, M. A. Małecka, P Kraszkiewicz, W. Mišta, O. Bezkrovnyi, L. Chinchilla, S. Trasobares Confinement of nano-gold in 3D hierarchically structured gadolinium-doped ceria mesocrystal: synergistic effect of chemical composition and structural hierarchy in CO and propane oxidation. *Catal. Sci. Technol* 12, (2022) 7082 https://doi.org//10.1039/d2cy01214f

[3] V. Paolucci, J. De Santis, L. Lozzi, G. Giorgi, C. Cantalini, Layered amorphous *a*-SnO_2 gas sensors by controlled oxidation of 2D-$SnSe_2$, *Sensors & Actuators: B. Chemical* 350 (2022) 130890, https://doi.org/10.1016/j.snb.2021.130890

[4] G. Žerjav, M. Roškarič, J. Zavašnik, J. Kovač, A. Pintar, Effect of Au loading on Schottky barrier height in TiO_2+Au plasmonic photocatalysts, *Applied Surface Science*, 579 (2022) 152196, https://doi.org/10.1016/j.apsusc.2021.152196

[5] L. Cabrera-Correa, L. González-Rovira, J. López-Castro, M. Castillo-Rodríguez, F. J. Botana. Effect of the heat treatment on the mechanical properties and microstructure of Scalmalloy® manufactured by Selective Laser Melting (SLM) under certified conditions. *Materials Characterization* 196, (2023), 112549. https://doi.org/10.1016/j.matchar.2022.112549

[6] J. K. Morzy, W. M. Dose, P. E. Vullum, M. C. Lai, A. Mahadevegowda, M. F. L. De Volder, C. Ducati. Origins and importance of intragranular cracking in layered lithium transition metal oxide cathodes, submitted December (2022)

[7] J.K. Morzy, PhD thesis, University of Cambridge (2022)

[8] A. Šestan, L. Sreekala, S. Markelj, M. Kelemen, J. Zavašnik, C. H. Liebscher, G. Dehm, T. Hickel, M. Čeh, S. Novak, P.Jenuš, Non-uniform He bubble formation in W/W_2C composite: Experimental and *ab-initio* study, *Acta Materialia*, 226 (2022) 117608, https://doi.org/10.1016/j.actamat.2021.117608

[9] I. Zrinski, J. Zavašnik, J. Duchoslav, A.W. Hassel, A. I. Mardare, Threshold Switching in Forming-Free Anodic Memristors Grown on Hf–Nb Combinatorial Thin-Film Alloys, Nanomaterials **2022**, 12, 3944, https://doi.org/10.3390/nano12223944

[10] *J. Morzy,* A. Sartor, W. M. Dose, C. Ou, S. Kar-Narayan, M. F. L. De Volder, and C. Ducati, Aerosol Jet Printing as a Versatile Sample Preparation Method for Operando Electrochemical TEM Microdevices *Adv. Mater. Interfaces* (2022), 2200530 https://doi.org /10.1002/admi.202200530.

DRAFT VERSION